Primate Saccade Rhythmicity

Tim Näher[1,2,3,*], Yufeng Zhang[1,2,3,4,*], Silvia Spadacenta[5,6], Martina Pandinelli[2,3], Lisa Bastian[7,8], Peter Thier[5,6], Ziad M. Hafed[5,6] & Pascal Fries[1,2,3]

1 Max-Planck-Institute for Biological Cybernetics, Tübingen, Germany

2 Donders Institute for Brain, Cognition and Behaviour, Radboud University, Nijmegen, Netherlands.

3 Ernst Strüngmann Institute (ESI) for Neuroscience in Cooperation with Max Planck Society, Frankfurt, Germany.

4 International Max Planck Research School for Neural Circuits, Frankfurt, Germany

5 Werner Reichardt Centre for Integrative Neuroscience, University of Tübingen, Tübingen, Germany

6 Hertie Institute for Clinical Brain Research, University of Tübingen, Tübingen, Germany

7 Institute for Medical Psychology and Behavioral Neurobiology, University Tübingen, Germany

8 Max Planck School of Cognition, Leipzig, Germany

* Contributed equally

Corresponding authors: tim.naeher@gmail.com

Abstract

Rhythmic sampling is a hallmark of many sensory systems in many diverse organisms. In primate vision, rapid foveating eye movements continuously scan the visual environment at a rate of 2-6 Hz, but the statistics of inter-saccadic interval distributions could equally well be described by non-rhythmic stochastic processes as by a (putatively variable) rhythmic oscillator. This raises the fundamental question whether primate visual scanning actually differs from the numerous examples of rhythmic sampling strategies exhibited across species and sensory modalities. Here, using experiments in humans, macaques, and a marmoset, as well as statistical approaches inspired by studies of temporal structure in neuronal spiking patterns, we show that primate saccade generation is unambiguously rooted in a rhythmic source. This finding was remarkably consistent across the three primate species despite their significant evolutionary distance. We find that saccade rate undergoes smooth, slow fluctuations. Accounting for those rate fluctuations was crucial for revealing the true degree of saccade rhythmicity. Thus, exact saccade timing is determined by an interaction between the slow saccade-rate fluctuations with the more temporally-local rhythmic generator. This demonstration of rhythmicity in overt oculomotor sampling behavior provides a link to the fundamental rhythmic nature of many central perceptual and cognitive processes, and places primate saccadic sampling into the large family of rhythmic active sampling behaviors.

Introduction

Vision is an active process: rather than passively receiving stimuli, organisms actively reposition their eyes to selectively sample behaviorally relevant information from the environment. In primates, saccadic eye movements shift the fovea to successive locations, creating a sequence of high-acuity "snapshots". During natural viewing, saccades occur repetitively, with inter-saccadic intervals (ISIs) of a few hundred milliseconds, yielding mean saccade rates of 2–6 Hz[1]. This repetitive sampling bears a striking resemblance to other active-sensing behaviors such as whisking and sniffing in rodents [2]. Those behaviors are known to be strongly rhythmic, raising the question of whether similar intrinsic rhythmic processes also govern saccade generation[3].

Several influential accounts of saccade behavior have, in fact, implicitly contained or predicted some degree of rhythmicity in the saccadic system. Classical descriptions of the temporal structure of saccades emphasized two temporal regularities: a refractory period following each saccade, during which the probability of initiating the next movement is suppressed, and a unimodal shape of the ISI distribution[4]. Both of these saccade characteristics can be explained by a saccade generation model based on a repetitive rise-to-threshold accumulation. Together, this implies that saccades show distinct temporal structure.

However, detailed inspection of saccade timing patterns reveals large variability in observed ISIs across many behavioral tasks, resulting in heavily skewed ISI distributions with substantial tails produced by fairly long ISI values. Such skew significantly complicates the interpretation of saccade timing as a rhythmic process, with some accounts even going as far as arguing that skewed ISI distributions are a manifestation of a non-rhythmic stochastic process governing saccade generation [5]. This, if true, would challenge prevailing assumptions about the strong links between eye movements and cognitive processes like attention[6–9] and visual sensitivity[10,11], which are themselves believed to be strongly rhythmic. Therefore, demonstrating, and understanding the properties of saccade-system rhythmicity is a fundamental problem in primate systems neuroscience.

In this work, inspired by statistical analysis approaches historically used to study temporal dynamics in neuronal spiking, we demonstrate genuine saccade-system rhythmicity in the primate brain. Using experiments with humans, macaques and a marmoset performing the same visual tasks, we show that high rhythmicity can still give rise to skewed ISI distributions when coupled with slow fluctuations in saccade rate, putatively due to factors like arousal, scene statistics, or task context. Critically, differences in apparent rhythmicity across tasks and species are driven by how neuronal circuits adjust saccade rate in response to task demands, not by changes in the regularity of the underlying generator. These findings reconcile previous conflicting accounts of saccade timing and demonstrate that a locally rhythmic generator does exist for saccades. Beyond providing a link between rhythmicity in covert attentional sampling and overt saccadic sampling, our results motivate investigation into the neuronal mechanisms underlying rhythmic saccade drive.

Methods

Participants and animals

Two adult rhesus macaques (*Macaque mulatta*, denoted C and G in the main text, both 19 years old) participated in this study. Both animals were implanted with a titanium headpost. Monkey G had a recording chamber implanted for addressing other scientific questions. To maintain motivation during the behavioral task, a small juice reward was given after each correct trial.

One adult marmoset (*Callithrix jacchus,* 6 years old) participated in the study.

Twenty-five adult human participants (12 males, 13 females), recruited from the public, participated in the current study. We excluded three participants (all female) due to insufficient number of trials. All human participants had normal vision and provided informed consent before participation.

Tasks

Figure 1 illustrates the stimuli. Importantly, all species performed the same tasks with only minor differences in the reward procedure (auditory feedback for humans versus juice delivery for macaques and marmoset).

Macaque task

Macaques were recorded in two types of sessions. Each type of session contained a specific set of tasks.

Session type 1 consisted of the REGULAR and IRREGULAR tasks. Each trial in both tasks began with the animal fixating at the center of the screen on a fixation dot (diameter 0.1 dva, i.e. degrees of visual angle). After fixation for 800 to 1000 ms, the fixation dot was turned off, followed by a ≈100 ms gap. The search array was then presented. The array consisted of white filled dots (diameter 0.3 dva) that reflected potential saccade targets (see Figure 1 for an illustration). Within the search array, 20% of the presented dots were real targets. The animal's task was to sequentially look at the dots to find any one of the real targets (foraging). During the foraging, if the animal's gaze landed inside a fixation window around a real target (radius 1.0 dva, not visible to the monkey), that target was replaced by an image of grapes, and a small juice reward was provided. If the monkey kept fixation on the grapes, multiple pulses of reward were provided every 200 ms until a maximum window of 2000 ms had passed. This was followed by an inter-trial interval of 500 ms and the start of a new trial with the presentation of a new fixation point. If the maximum search time passed (5000 ms) and none of the real targets had been foveated, the trial was terminated without a reward, followed by the same inter-trial interval and the start of a new trial. In the REGULAR task, the dots in the search array were spaced as if they were the centers of an invisible hexagonal tiling. In the IRREGULAR task, the search array contained the same number of dots as in a REGULAR trial, but the positions of the dots were randomly redistributed across the full screen to break any spatial regularity.

Session type 2 consisted of only one task, the IMAGE task, and began with the animal fixating at the central fixation dot. This pre-search fixation for the IMAGE task was identical to the REGULAR or IRREGULAR tasks. After fixation for 800 to 1000 ms, the fixation dot was turned off, and after a ~100 ms gap, it was replaced by a natural image in color (16 * 21 dva, McGill

Calibrated Colour Image Database, http://tabby.vision.mcgill.ca). From the moment the fixation dot was turned off, the animal was free to explore the image. After a random delay of 100 ms to 1900 ms, a small white dot (either 0.1 dva radius or 1.7 dva radius, randomly interleaved), the target, appeared at a random location within the image. We used two different radii for a comparison that is not relevant to the current study. The monkey's task was to locate this target within a period of 5000 ms. If the target dot was found, the reward procedure as described for session type 1 followed.

Marmoset task

The marmoset task closely mirrored the macaque version, with parameter adjustments to accommodate species-specific behavioral and attentional constraints. The key differences are described below.

All three tasks (REGULAR, IRREGULAR, and IMAGE) were presented within a single session type, in random order. Each trial began with fixation on a central red dot (diameter 0.4 dva) which the animal had to acquire within 200 ms and hold for up to 600 ms. The fixation dot was then turned off and followed by a ~100 ms gap. In the REGULAR and IRREGULAR task, the search array was then presented. Array composition, target proportion (20%), dot spacing rules, and maximum search time (5000 ms) were identical to the macaque version.

The fixation window around real targets was enlarged (2 x 2 dva, not visible to the monkey) to reduce frustration and encourage longer working times. Upon successful target fixation, the target was replaced by an image of a marmoset face (3 × 4 dva), and a small amount of marshmallow juice was delivered. If the monkey kept fixation on the marmoset face, short pulses of reward were provided manually until trial end.

For the IMAGE task, stimuli (16 x 21 dva) were drawn from the same database. Only a single target size was used (diameter 0.3 dva, white). The monkey's task was to locate this target within a period of 5000 ms. If the target dot was found, multiple pulses of reward were manually provided until a maximum window of 3000 ms had passed.

Note that due to a bug in the stimulation script, the end-of-trial marker was missing in the marmoset data. We therefore decided on a fixed trial length of 4 s in which most marmosets found the reward.

Human tasks

Human participants were recorded in two types of sessions. Each type of session contained a specific set of tasks.

Session type 1 consisted of the REGULAR, IRREGULAR, and IMAGE tasks. These tasks for human participants were identical to the respective tasks for macaques, except for the following differences: (1) The pre-search fixation duration was 2500 to 3500 ms; (2) the post-search fixation duration was also 2500 to 3500 ms and did not contain a repetitive reward; (3) in all tasks, successful trial completion was indicated by a short audio feedback. If the maximum search time passed and no target was found, the trial was terminated. Inter-trial-intervals were 2000 ms.

Session type 2 included the REGULAR and IMAGE tasks, as well as the free-viewing MOVIE task. It was identical to session type 1, except for the following differences: (1) The REGULAR task in session type 2 contained three different spacings of the grid (hexagon radius of 2.3,

4.5, and 8.5 dva); (2) the IMAGE task remained unchanged from session type 1 despite a different set of images being used.

The free-viewing MOVIE task (performed exclusively by human participants) consisted of a 10-minute naturalistic first-person-view video. The video contained minimal cuts, such that uninterrupted epochs lasted several minutes. Furthermore, the camera trajectory was smooth, minimizing transients due to camera movement. The movie is in color, was downloaded from YouTube (https://www.youtube.com/watch?v=hld4uaO1MDE) and can be obtained from the authors upon request. We chose this movie, because it provides naturalistic visual content, motivates subjects to sustained saccadic exploration of the continually renewing input, and largely avoids transients. Participants were instructed to keep their head still on the chinrest and simply watch the movie without performing a specific task.

Eye Movement Recording

All visual stimulation was controlled by custom software (https://github.com/esi-neuroscience/ARCADE) and presented on an LCD monitor. For macaques, the monitor was an LG 32GK850G-B with a refresh rate of 143.9 Hz. For marmoset monkeys, the monitor was a 10 Inch Beetronics with a refresh rate of 60 Hz. For human participants, the monitor was a ViewPixx (VPixx Technologies Inc) with a refresh rate of 120 Hz. In humans and macaques, we recorded binocular gaze data at 500 Hz using an EyeLink-1000 system (SR Research Ltd.). For marmoset monkey, we recorded monocular gaze data at 120 Hz using an ISCAN ETL-200 infrared eye tracking system. All gaze data were up-sampled to 1 kHz to achieve a common sampling rate for all further analyses. Real-time gaze data from one eye was utilized for online behavioral control such as the pre- and post-search fixation periods.

The human data were collected across one or two sessions, with some participants attending only the first session and others attending both. The first session included a brief training block to ensure participants gained experience with the online eye-tracking control and to fully understand the task. A given session encompassed up to six blocks with the REGULAR, IRREGULAR, and IMAGE tasks randomly interleaved. Each block consisted of 60 trials, 20 of each task. Participants worked on one block until 60 correct trials (20 of each condition) were achieved. Participants were encouraged to complete all six blocks; however, the total number completed was contingent upon each participant's level of fatigue. The experimental design sought to prioritize participant comfort and data accuracy over the volume of completed blocks. The second session used the same approach, but for session type 2.

Saccade detection

We used a convolutional neural network (CNN) for saccade detection[12]. We trained separate networks for humans, macaques, and the marmoset on randomly selected trials from each species. First, we labeled saccades and fixations as separate classes in the data using a custom GUI. After epoching the data into trials, we replaced blinks with NaNs. Subsequently, we used those preprocessed data to train the CNN, then detected saccades for each eye separately. We only accepted saccades if they occurred in both eyes simultaneously. For all detected saccades, we enforced a minimum duration of 6 ms and a minimum separation between two subsequent saccades of 15 ms.

Trial-wise saccade rates

For all further analyses of the trial-based conditions (i.e. REGULAR, IRREGULAR, IMAGE, but not MOVIE), only trials with a minimum duration of 1 s were included.

A central aspect of the analysis will be concerned with saccade rates. For the trial-based conditions, we computed the mean saccade rate for each trial and used this to quantify between-trial variability in saccade rate. Saccade rate was computed as the total number of detected saccades within the trial divided by the trial duration in seconds, after excluding the initial 100 ms post stimulus onset, because saccade rates are known to show a transient decrease after fixation or stimulus onset[13–16]. Trial-wise saccade rates were used for all analyses relating saccade rate to the rate-corrected rhythmicity index (RCRI, see below), including rate stratification and regression analyses.

Gamma renewal modeling with time-varying rate

To investigate whether heavy-tailed inter-saccadic-interval (ISI) distributions can arise from a locally regular (i.e. rhythmic) generator operating under time-varying saccade rate, we fitted a gamma renewal model in which the shape of the ISI distribution is fixed within a subject, while the mean of each ISI distribution is determined by the trial-wise rate. The details of such fitting are provided below.

For each subject (humans, macaques, and marmoset), we extracted all valid ISIs. For model fitting and visualization, all analyses used ISIs within 100–600 ms range, thereby matching the range that we used for histogram-based comparisons.

Local rate estimation

To capture the rate variability, we estimated the local saccade rate associated with each ISI using a sliding window of width $W = 1$s. Let t_i and t_{i+1} denote the onset times (in seconds) of two successive saccades, and $\Delta t_i = t_{i+1} - t_i$ the corresponding ISI. We assigned to each ISI a midpoint time $m_i = (t_i + t_{i+1})/2$. The local rate r_i was computed as the number of saccades whose onset times fell within $[m_i - W/2,\ m_i + W/2]$ divided by the actual window duration after truncation at the trial boundaries.

Gamma renewal model with rate-dependent mean

We modelled each Δt_i, i.e. each ISI, as an independent draw from a gamma distribution with a single subject-specific shape parameter k and a rate parameter β_i determined by the local rate r_i. Specifically, the model imposes a local mean interval

$$\mathbb{E}[\Delta t_i] = \frac{1}{r_i}$$

and uses the gamma parameterization in which mean $= k/\beta_i$. Thus, the rate parameter varies across ISIs as

$$\beta_i = k r_i$$

To estimate k without making assumptions about the precise time course of the local rate, we exploited the time-rescaling theorem. If the model is correct, the rescaled variables

$$z_i = r_i \cdot \Delta t_i \sim \text{Gamma}(k, k)$$

regardless of how r_i varies across ISIs. We therefore estimated the local rate at the trial level as $\hat{r} = n_{\text{filt}}/T_{\text{filt}}$, where n_{filt} is the number of ISIs and T_{filt} is their total duration in seconds. We then formed $z_i = \hat{r} \cdot \Delta t_i$ for all ISIs within that range and fitted a gamma distribution to the pooled z values by maximum likelihood yielding $\hat{k}$ and its standard error from the Fisher information. Goodness of fit was assessed with percentile–percentile (PP) plots of the empirical z values against the fitted $\text{Gamma}(\hat{k}, \hat{k})$ distribution, as well as formally with a one-sample Kolmogorov–Smirnov (KS) test comparing the empirical distribution of z to the fitted gamma CDF; a non-significant KS statistic indicates that the data are consistent with the model.

To interpret the fitted shape parameter, we define "high" k in terms of the skewness of the local gamma ISI distribution. For a $\text{Gamma}(k, \beta_i)$ distribution, the skewness depends only on the shape and is given by

$$\text{Skew}(\Delta t) = \frac{2}{\sqrt{k}}.$$

We take "mildly skewed" to mean $\text{Skew}(\Delta t) \leq 0.75$, which implies

$$\frac{2}{\sqrt{k}} \leq 0.75 \quad \Rightarrow \quad \sqrt{k} \geq \frac{8}{3} \quad \Rightarrow \quad k \geq \frac{64}{9} \approx 7.1.$$

Thus, throughout we refer to $k \geq 8$ as a high gamma shape parameter under this criterion, corresponding to a locally only mildly right-skewed ISI distribution.

Rate-corrected ISI distribution

To visualize the structure of ISI variability after accounting for trial-level rate fluctuations, we computed a rate-corrected ISI for every empirical ISI. For each $\Delta t_{i,j}$ (the *j*-th ISI in trial *i*) with associated local rate estimate r_i, we formed the dimensionless ratio

$$z_{i,j} = r_i \cdot \Delta t_{i,j}$$

which expresses each ISI as a multiple of the expected interval $1/r_i$ at that local rate. Under the gamma renewal model, $z_i \sim \text{Gamma}(k, k)$ with mean 1, so this rescaling removes between-trial rate differences while preserving within-trial ISI variability. Rescaled ISIs were pooled within each species and their distributions visualized as kernel density estimates.

Rate-corrected rhythmicity measure

To quantify local rhythmic regularity while minimizing sensitivity to slow rate fluctuations, we used a rate-corrected rhythmicity index, $RCRI$, based on the local variation of successive ISIs.

Local variability was quantified using the CV_2 statistic, defined for successive ISIs as

$$\mathrm{CV}_2(i,j) = \frac{2\left|\Delta t_{i,j+1} - \Delta t_{i,j}\right|}{\Delta t_{i,j+1} + \Delta t_{i,j}}.$$

The overall local variation was computed as the mean across intervals, $CV_2 = \langle CV_2(i) \rangle$. The rate-corrected rhythmicity index was then defined as

$$RCRI = \frac{1}{1 + CV_2}.$$

For a Poisson process with exponentially distributed ISIs, the expected value of CV_2 is 1, yielding $RCRI = 0.5$. Values of $RCRI > 0.5$ therefore indicate greater local regularity than expected from a Poisson process. Furthermore, RCRI is analytically scale-invariant: because CV_2 is a ratio of differences to sums of consecutive ISIs, multiplying all intervals by a constant c leaves the index unchanged (the factor c cancels in numerator and denominator), making it independent of absolute saccade rate.

The CV_2 statistic and related local variation measures are widely used in neuronal spike-train analysis to quantify firing regularity under non-stationary conditions, where mean firing rates may vary over time[17]. Because CV_2 depends only on pairs of successive intervals, it is less sensitive to slow changes in mean rate.

Stationary vs non-stationary processes and spectral measures

To isolate the effects of slow rate fluctuations on rhythmicity metrics and spectral measures, we simulated event sequences using stationary and non-stationary gamma renewal processes that were matched in local regularity but differed in their rate dynamics.

In both simulations, saccade times were generated as a gamma renewal process, in which successive ISIs were drawn independently from a gamma distribution. Local regularity was held constant by fixing the coefficient of variation of the ISI distribution to $CV = 0.15$, corresponding to a highly regular, oscillator-like generator.

In the stationary process, the mean ISI was fixed by setting a constant rate equal to the mean of an empirical rate time course derived from the MOVIE task, resulting in a time-invariant ISI distribution.

In the non-stationary process, the mean ISI varied over time according to that same empirical rate time course from the MOVIE task. At each step, the rate of the gamma process was set to the inverse of the current empirical rate, while the shape of the distribution, and thus local regularity, was kept constant. As a result, ISIs were locally regular but globally heterogeneous due to slow rate fluctuations present in the empirical rate dynamics.

Spectral analysis of event trains

To quantify rhythmicity with spectral measures, simulated event times were discretized into a binary event train at 1 ms resolution (sampling frequency 1000 Hz). Power spectral density (PSD) estimates were computed using Welch's method (segment length 2048 samples, constant detrending, density scaling).

For each simulation, we extracted the maximum PSD value within the 2–6 Hz frequency range ("peak power") as a summary measure of spectral rhythmicity[5].

We generated multiple (n = 500) independent realizations of the stationary and non-stationary processes. For each realization, we extracted the peak power in the 2–6 Hz range and the $RCRI$ computed from the simulated ISIs.

Rate-stratified analysis of saccade rhythmicity

To assess the relationship between saccade rate and rhythmic structure using a nonparametric approach, we performed a rate-stratified analysis within each species separately. For each trial, mean saccade rate was computed as defined earlier.

Within each species, trials were ranked by mean saccade rate and assigned to tertiles (low, medium, high) using quantile binning, ensuring equal numbers of trials per bin. This procedure controlled for differences in saccade rate across species and allowed rate-dependent effects to be examined within comparable relative rate ranges.

For each species and rate bin, saccade autocorrelation functions were computed and then averaged across trials within each bin. Additionally, ISI distributions were obtained by pooling ISIs across trials within the bin. Within each species, trial-wise rate-corrected rhythmicity values (as defined above) were grouped by rate bin.

For humans, pairwise comparisons of rhythmicity between rate bins were performed using independent-samples *t*-tests. For macaques and marmoset, where trials were pooled across individuals[18], pairwise comparisons were performed using two-sided Mann–Whitney U tests. All statistical tests were conducted within species, and significance was assessed at $\alpha = 0.05$.

Within-trial slow rate fluctuations and induced higher-order dependencies

Windowed saccade-rate estimates

Within each MOVIE trial, saccade onset times were binned into non-overlapping windows of 3 s. For each window, saccade rate was computed as the number of saccades divided by window duration (Hz), yielding a within-trial rate time series.

Blinks were identified as time segments in which eye-position samples contained NaNs. For analyses based on ISIs, any ISI which overlapped a blink segment was excluded.

For each trial, we computed the lagged serial correlation of the windowed saccade-rate time series for lags up to 20. Serial correlation functions were then averaged across trials.

To characterize the frequency content of within-trial rate fluctuations, we estimated the power spectral density of the windowed rate series using Welch's method. Because rate was sampled once per 3 s window, the effective sampling frequency was 1/3 Hz.

Monte Carlo null model for rate autocorrelation

To test rate autocorrelations against a memoryless baseline, we constructed a per-trial surrogate under a homogeneous Poisson null while preserving each trial's total saccade count. For each eligible trial with N_i saccades and B_i windows, surrogate window counts were generated via a multinomial draw with uniform bin probability $1/B_i$. Surrogate rates were computed as counts divided by 3 s. The autocorrelations were computed identically to the empirical data.

This procedure was repeated 500 times. For each lag, we derived a 95% null envelope based on the 2.5th–97.5th percentiles.

ISI serial correlations

For each trial, we again computed the ISI sequence as the difference between successive saccade onset times (see above). Higher-order temporal dependencies were quantified using lagged serial correlations across the ISI sequence: for lag k, the correlation between ISI_n and ISI_{n+k} was computed for $k = 1, \dots, 20$. Correlation functions were averaged across trials.

Rate-conditioning via integrated intensity transformation

To assess ISI serial correlations after conditioning on within-trial rate fluctuations, we applied a time-rescaling transformation using the trial's windowed rate estimate. This rescaling allows us to analyze ISI time courses, while removing correlations introduced by rate fluctuations.

1. The windowed rate series was linearly interpolated to obtain a continuous rate function $\lambda(t)$, with $\lambda(t) \geq 0$.
2. For each ISI spanning $[t_n, t_{n+1}]$, we computed the integrated intensity

$$\Lambda_n = \int_{t_n}^{t_{n+1}} \lambda(t)\, dt,$$

   using numerical integration with a step size of 0.01 s. Importantly, Λ_n gives the duration of the interval $[t_n, t_{n+1}]$ measured in rescaled (intensity) time. This transformation expresses each ISI in units of expected event count, thereby removing correlations induced solely by slow rate fluctuations.
3. Serial correlations were then recomputed on the transformed interval sequence $\{\Lambda_n\}$ using the same lag range (1–20).

Drift-to-threshold model

To formalize the relationship between saccade rate and rhythmicity, we implemented a drift-to-threshold model (Figure 7; similar to LATER models)[4]. In this model, a decision variable accumulates linearly with drift rate μ and additive Gaussian noise (diffusion coefficient σ) toward a fixed threshold ϑ. Upon threshold crossing, a saccade is triggered, and the accumulator resets to zero, followed by a fixed refractory period τ. The resulting inter-saccade intervals follow an inverse Gaussian distribution with mean ϑ/μ and shape ϑ^2/σ^2, shifted by τ. We fixed the threshold at $\vartheta = 1$ (arbitrary units) and the refractory period at $\tau = 50$ ms, and fitted the single remaining free parameter σ to the scatter plot of RCRIs as function of empirical rates, as presented in Figure 4, by minimizing the sum of squared errors. For each

empirical saccade rate r, the corresponding drift was determined analytically as $\mu = \vartheta / (1/r - \tau)$. Predicted RCRI values were computed deterministically via numerical integration over the inverse Gaussian probability density function on a 500-point grid. To illustrate how natural rate fluctuations affect rhythmicity, we additionally simulated an accumulator driven by a time-varying drift signal with $1/f$ spectrum, producing a continuous mixture of saccade rates between 1.5 and 4.8 Hz.

Statistical analyses

To assess whether trial-wise saccadic rhythmicity could be explained by saccade rate, we performed species-specific linear regression analyses using ordinary least squares. The dependent variable was trial-wise RCRI, as defined above. Mean saccade rate (Hz) was computed for each trial as the number of saccades divided by trial duration.

For each species, rhythmicity was modelled as a function of mean saccade rate and experimental task. Task was included as a categorical predictor with three levels (REGULAR, IRREGULAR, IMAGE).

For humans, additional comparisons of rhythmicity across rate-defined bins were performed using independent-samples *t*-tests. For macaques and marmosets, where data were pooled across individuals, comparisons were performed using two-sided Mann–Whitney U tests.

Unless otherwise stated, all statistical significances were assessed at $\alpha = 0.05$. All analyses were conducted in Python 3.11 using NumPy (v1.24), pandas (v2.0), SciPy (v1.11), and *statsmodels* (v0.14).

Ethics statement

Humans

The study was approved by the local ethics committee (Ethikkommission des Fachbereichs Medizin der Goethe-Universität, Nr 2022-1031_1-). Participants gave written consent before participating in the study.

Macaques

All procedures and housing conditions complied with the German and European law for the protection of animals (EU Directive 2010/63/EU for animal experiments). All surgical and experimental methods were approved by the regional authority (Regierungspräsidium Darmstadt) under the following permit numbers: F149-1008 & F149-1007. To support their wellbeing, animals were offered dietary variety, habitat enhancements, and interactive objects.

Marmosets

All experimental protocols were approved by the local animal care committee (Regierungspräsidium Tübingen, Abteilung Tierschutz) and fully complied with the German and European law for the protection of animals (EU Directive 2010/63/EU for animal experiments).

Results

We characterized the nature of saccade rhythmicity in three primate species by having them view static or dynamic scenes (Figure 1). In each case, we assessed to what extent the timing between successive saccades (ISI) could be thought of as being generated by a rhythmic process, and we did so by relating such timing to slower saccade rate fluctuations. We hypothesized that ISI distributions can be effectively modeled as a doubly-stochastic process, with one component governed largely by a relatively regular oscillator, and another component that slowly alters the period of the oscillator (and thus the overall saccade rate). In what follows, we first show that saccade rate substantially fluctuates in all three species, and we then explain how accounting for such fluctuations reveals the degree of intrinsic rhythmicity in saccades.

Saccade rates vary across trials

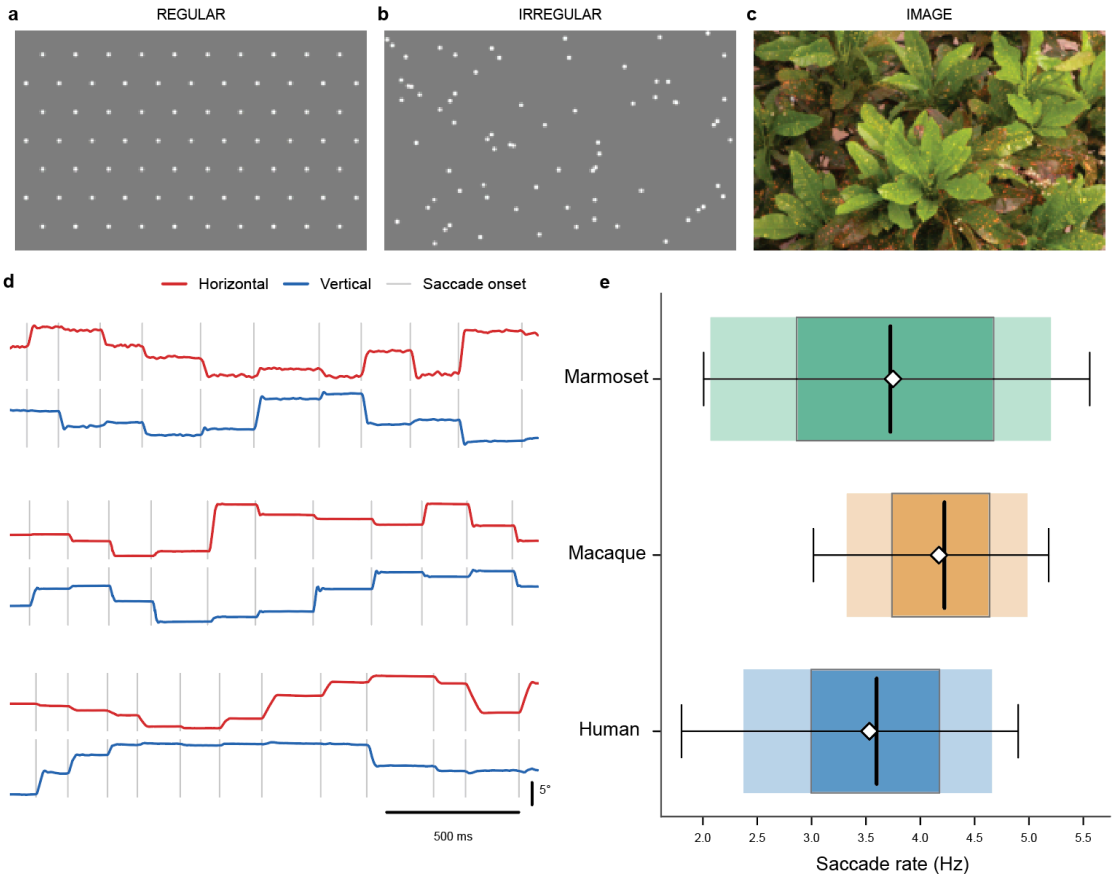

Figure 1: Saccade rates vary across trials. (a-c) Example task screens of the three conditions: REGULAR, IRREGULAR, and IMAGE. These conditions were used for all analyses in this figure. **(d)** Example eye traces from all three species. Detected saccade onsets are indicated by vertical lines. Temporal scale bar indicates 500ms, vertical scale bar 5 degree of visual angle. **(e)** Box plots reflecting the distributions of saccade rates over trials. Trials were pooled over conditions (REGULAR, IRREGULAR, and IMAGE) and subjects, separately for the three species. Median [interquartile] rates were 3.60 [3.00, 4.18] Hz (human, n = 22 subjects), 4.22 [3.74, 4.64] Hz (macaque, n = 2 subjects), and 3.73 [2.86, 4.68] Hz (marmoset, n = 1 subject). The 5th–95th percentile ranges were 1.80–4.90 Hz, 3.02–5.18 Hz, and 2.01–5.56 Hz, respectively. The darker shaded box spans the interquartile range (25th–75th percentile), the lighter shaded region extends from the 10th to 90th percentile, the vertical

black line marks the median, the white diamond indicates the mean, and the whiskers with caps denote the 5th–95th percentile range. Mean ± SD of the saccade rates were 3.53 ± 0.95 Hz in humans, 4.17 ± 0.67 Hz in macaques, and 3.75 ± 1.18 Hz in marmosets. Saccade rate was computed per trial as the number of saccades divided by trial duration (s), after excluding the first 100 ms following array/image onset to minimize onset-transient effects.

We first quantified trial-to-trial variability in saccade rate across trials for the three investigated species: human, macaque and marmoset. For each species, saccade rates varied widely rather than clustering tightly around a single characteristic value (Figure 1e). In humans, trial-wise rates spanned nearly 3 Hz across the central 90% of trials (mean ± SD: 3.53 ± 0.95 Hz, 5th–95th percentile: 1.80–4.90), indicating substantial variability. Macaques showed a similarly broad distribution (mean ± SD: 4.17 ± 0.67 Hz, 5th–95th percentile: 3.02–5.18), while the marmoset exhibited the largest relative spread (mean ± SD: 3.75 ± 1.18 Hz, 5th–95th percentile: 2.01–5.56). Thus, in all three species, saccade rates varied substantially from trial to trial, indicating that the underlying process cannot be modeled with a single stationary rate.

Gamma renewal models can reproduce heavy-tailed ISI distributions

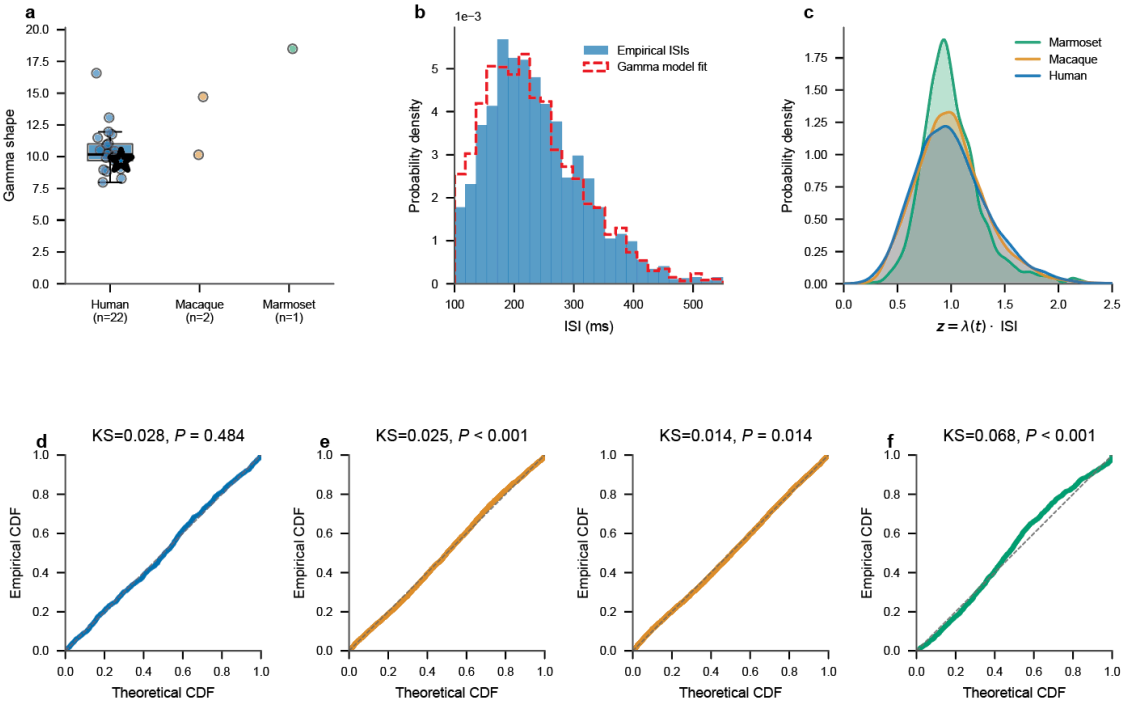

Figure 2: Gamma renewal models can reproduce heavy-tailed ISI distributions. Saccade rates were determined empirically per trial and used to normalize the trial-wise ISIs. The normalized ISIs were pooled over trials and conditions, per participant, and the resulting distributions were fitted with a gamma renewal model with the shape parameter as the only free parameter. **(a)** Fitted gamma-shape parameters. Points indicate individual participants; the star indicates the example participant in panel **b**. The overall large shape-parameter values indicate strong local regularity: after accounting for trial-wise saccade rate, the rate-normalized ISIs are near-symmetric (skew ≤ 0.75). **(b)** Blue: Empirical ISI distribution from the example human participant. Red: Best-fitting gamma-renewal model; The model reproduces the heavy-tail ISI distribution, despite being locally regular with a gamma shape parameter value close to ten. **(c)** Rate-corrected residual kernel density ISI distributions after correcting per trial for the expected value of ISI, separately for all three species. **(d)** Example human probability-probability (PP) plot, showing that rate-corrected ISI distributions follow the proposed gamma distribution shape. For humans, all KS-tests were non-significant, indicating that the gamma model is a good fit. **(e)** same as **d**, but for the two macaques. **(f)** same as in **e**, but for the marmoset. Note that the KS tests were significant for the macaques and the marmoset.

The large trial-to-trial variability in saccade rate observed in all tested species (Figure 1) has two important implications for the interpretation of saccade timing statistics. First, the empirically observed heavy-tailed inter-saccadic-interval (ISI) distribution reflects a marginal distribution aggregated over time, rather than the interval statistics generated at any fixed moment. When saccade rate varies, the overall ISI distribution becomes a mixture of many locally generated interval distributions with different means, such that heavy tails can arise even if saccades are generated by a locally regular process. Second, rate fluctuations can introduce higher-order temporal structure that can affect spectral analyses of saccade rhythmicity.

To test these implications explicitly, we modeled saccade generation as a doubly stochastic gamma renewal process, with temporally local stochasticity and a time-varying rate. These saccade rates were determined empirically per trial. Using the time-rescaling theorem, we

rescaled each ISI by its trial-wise rate to obtain normalized ISIs. The normalized ISIs were pooled over trials and conditions, per participant. The resulting distributions were fitted with gamma distributions, where the only free parameter was the shape parameter k.

In humans, fitted k values were 10.49 ± 1.78 (5th–95th percentile: 8.31–13.02; min–max: 7.98–16.57). Macaques showed similar values (12.43 ± 2.28; 5th–95th percentile: 10.38–14.48; min–max: 10.15–14.71). The marmoset data yielded a gamma shape parameter of 18.49. All fitted values exceeded the threshold of $k \geq 8$, corresponding to a local ISI distribution with skewness ≤ 0.75, indicating that distributions were only mildly right-skewed. Goodness of fit was assessed visually with probability-probability (PP) plots of the rescaled ISI distributions against the fitted gamma distributions, and statistically with one-sample Kolmogorov–Smirnov (KS) tests (Figure 2d-f). In humans, no individual KS test reached significance (mean KS = 0.030, mean $P = 0.558$ with 0/22 rejected at $\alpha = 0.05$), indicating that the gamma renewal model provided an excellent fit. In macaques, the KS tests were significant for both animals (monkey C: k = 14.7, KS = 0.025, $P < 0.001$; monkey G: k = 10.2, KS = 0.014, $P = 0.014$), and the marmoset likewise showed a significant deviation (k = 18.5, KS = 0.068, $P < 0.001$). To characterize the nature of these deviations, we compared the empirical variance, kurtosis, and quantile ranges of the rescaled ISIs against the predictions of the fitted gamma. In monkey C (k = 14.7), the central body was more concentrated than predicted (IQR 9% narrower than the fitted gamma IQR) while the extreme tails were wider (1st–99th percentile range 7% wider), and kurtosis exceeded the fitted gamma prediction (empirical: 1.54, fitted: 0.41), indicating a leptokurtic distribution, that is, a distribution with a sharper peak and heavier tails than the fitted gamma. In monkey G (k = 10.2), the KS rejection was marginal ($P = 0.014$) and quantile ranges matched the fitted gamma closely (all ratios 0.97–1.02). The significant KS test is therefore likely due to slight deviations from a pure gamma distribution combined with high statistical power provided by the large number of ISIs. The marmoset showed a similar pattern as monkey C, but even more pronounced (IQR 19% narrower, 1st–99th range 22% wider, excess kurtosis empirical: 3.49, fitted: 0.33). The leptokurtic pattern in monkey C and the marmoset is consistent with a highly regular core timing process plus few very long ISIs. Those very long ISIs might be due to the saccade-detection procedure missing a few saccades.

Figure 2c shows the distribution of ISIs after rescaling each interval by its local saccade rate, which removes rate variation across trials and isolates the local timing regularity of the saccadic rhythm.

Having established a substantial rhythmic component in primate saccade timing, we next asked how slow rate fluctuations affect spectral measures that have been used to assess saccade rhythmicity[5]. We simulated stationary and non-stationary gamma renewal processes that had similar local regularity and similar mean rates yet differed with regard to the presence or absence of rate fluctuations over time (Figure 3).

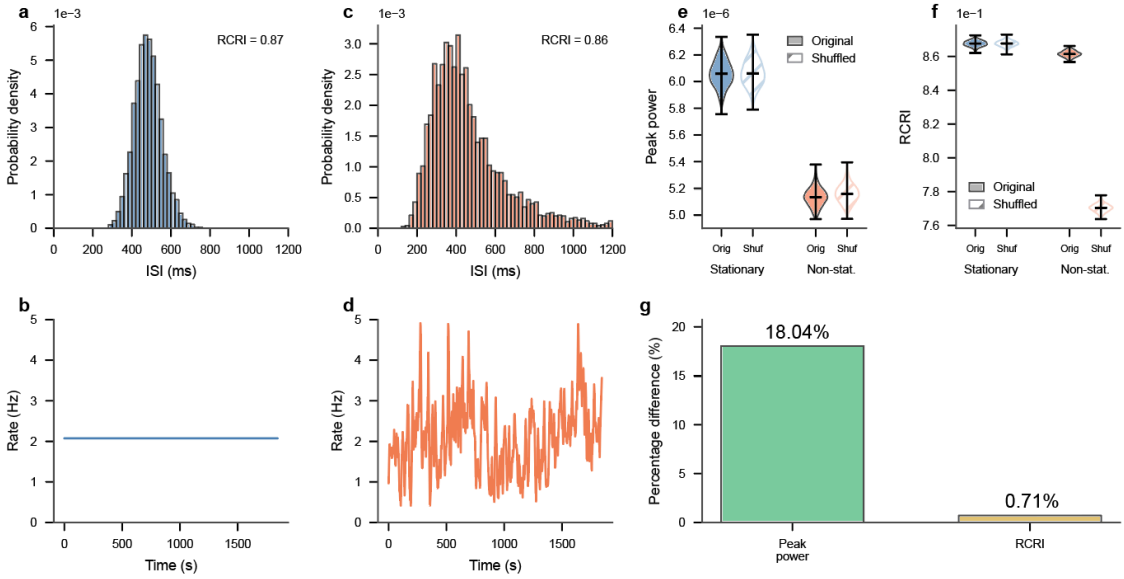

Figure 3: Slow rate fluctuations confound spectral rhythmicity measures. All panels show the results of simulations of gamma renewal processes with a fixed shape parameter of 44.4. **(a, b)** Example stationary gamma renewal process with fixed rate that is based on the mean of the time series in d. The resulting marginal ISI distribution is narrow and devoid of a heavy tail. Note that the x-axis scale in panel B is in seconds. (**c, d)** Example non-stationary gamma renewal process with an empirical rate time series from a free viewing trial of the MOVIE condition. The resulting marginal ISI distribution is heavy-tailed despite being based on the same shape parameter as panel a and thereby the same local interval regularity. Note that the x-axis scale in panel d is in seconds. **(e)** Peak power (2–6 Hz) across 500 simulations, comparing original and ISI-shuffled spike trains for both stationary and non-stationary gamma renewal processes. **(f)** Rate-corrected rhythmicity index (RCRI) for the same original and ISI-shuffled stationary and non-stationary processes across 500 simulations. Note that the y-axis is highly zoomed in and reveals that the RCRI is highly similar between the stationary and non-stationary process, and that shuffling strongly reduced RCRI as required for shuffling to be a valid control. **(g)** Percent difference between the same stationary and non-stationary processes in peak power (left) and RCRI (right).

Figure 3a,b shows an example stationary gamma renewal process with a shape parameter of 44.4 and a constant rate corresponding to the mean rate of the empirical rate time course shown in Figure 3d. This process produced a narrow ISI distribution, and a rate-corrected rhythmicity index (RCRI, see Methods) of 0.87, reflecting its strong local regularity. Figure 3c,d shows an example non-stationary gamma renewal process with a rate that followed a time course empirically observed during a long free-viewing MOVIE-condition trial. Despite producing a heavy-tailed ISI distribution (Figure 3c), the RCRI was nearly identical to the stationary process (RCRI = 0.86), indicating very similar local regularity once slow rate fluctuations were accounted for.

Repeating this simulation 500 times showed that spectral measures of rhythmicity, such as peak power[5], are strongly affected by rate changes (Figure 3e), while the RCRI is hardly affected (Figure 3f, note the highly zoomed-in y-axis). The rate-related difference is 18.04% for peak power, while it is merely 0.71% for the RCRI (Figure 3g).

An ISI-shuffled control within each condition (lighter violins in Figure 3e,f) revealed that peak power was unaffected by shuffling regardless of stationarity, demonstrating that spectral measures alone do not validly capture local temporal regularity in the face of slow rate

fluctuations. In contrast, RCRI dropped selectively after shuffling in the non-stationary condition while remaining invariant for the stationary process, confirming its sensitivity to the local serial dependencies imposed by rate modulation.

Together, Figures 2 and 3 show that two properties of the temporal dynamics of saccade generation, namely heavy-tailed ISI distributions and attenuated spectral peaks, can both arise from a locally regular saccade generator operating under a slowly varying rate. These slow rate fluctuations will be characterized in more detail later. In this framework, local rhythmicity of successive intervals is preserved, while slow rate fluctuations shape global interval statistics, such as the marginal ISI distribution, and introduce higher-order temporal structure that degrades standard spectral measures of rhythmicity. Having disentangled these rhythmic and rate-dependent components, we next used the RCRI to isolate the rhythmic component and compare it across tasks and species.

Saccade rate explains across-task differences in rhythmicity

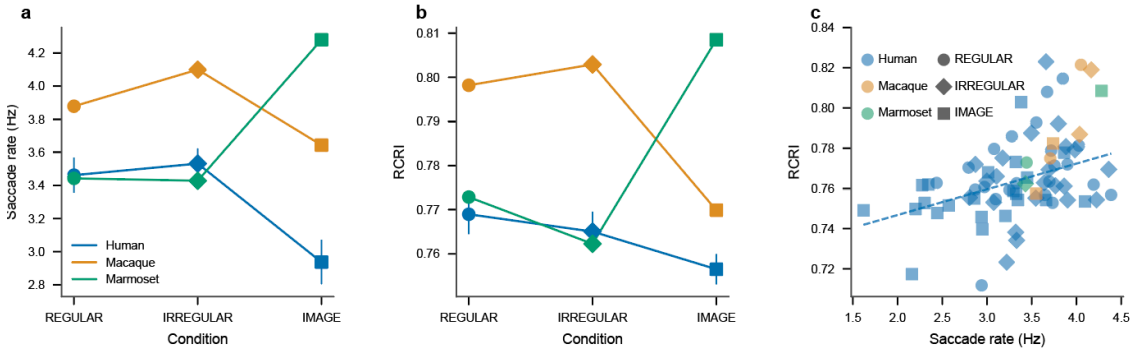

Figure 4: Saccade rates and RCRI across tasks and species. (a) Mean saccade rate across task conditions (REGULAR, IRREGULAR, IMAGE) for humans, macaques, and marmoset. Task context robustly modulates saccade rate in all species. **(b)** RCRI across the same conditions, showing condition-dependent changes that closely mirror saccade rates. **(c)** Relationship between saccade rate and RCRI for human data (blue symbols). Each symbol corresponds to the combination of a human participant and a task condition. Human data show a significant positive correlation (dashed line, based on human data only). Macaque and marmoset data were not included in the correlation analysis yet fall along the same trend. Importantly, RCRI is invariant to uniform scaling of ISIs (see Methods), meaning the positive correlation between rate and rhythmicity cannot arise from a trivial dependence of the RCRI metric on ISI duration.

So far, we have established that slow rate fluctuations shape ISI distributions and degrade spectral measures of saccade rhythmicity, and that the RCRI provides a robust estimate of local rhythmicity that is nearly immune to slow rate variability. Equipped with this metric, we investigated whether there is a genuine relationship between RCRI and saccade rates, across tasks and species, i.e., a relationship that is not due to a trivial rate confound of the metric but that reflects a true physiological rate dependence. We calculated RCRI for humans, macaques, and marmoset performing a visual foraging task in three conditions: a regular hexagonal grid (REGULAR), a spatially jittered version of the same grid (IRREGULAR), and a natural-image condition (IMAGE). This task design produced various inputs to the visual system by systematically varying spatial periodicity between the REGULAR and IRREGULAR conditions. To further enhance ecological validity, we added the naturalistic IMAGE condition.

Figure 4a shows average saccade rates across conditions for each species. In all species, saccade rates varied substantially between conditions, with the IMAGE condition generally eliciting lower saccade rates in humans and macaques, yet higher rates in the marmoset. Thus, task context robustly modulated saccade rate in all three species.

Figure 4b shows the corresponding RCRI values. Within each species, RCRI varied systematically with condition in a manner closely mirroring changes in saccade rate. Conditions associated with higher saccade rates also exhibited higher RCRI, whereas conditions with lower saccade rates showed reduced RCRI. This shared modulation suggests a genuine link between saccade rate and local saccade rhythmicity.

To quantify this relationship, we examined the association between saccade rate and RCRI. Figure 4c shows this relationship for human participants, with each dot corresponding to one of the tasks in one participant. This revealed a positive correlation between saccade rate and RCRI ($r = 0.39$, $P = 0.001$). The corresponding data points from the two macaques and the marmoset fall into the human point cloud, descriptively pointing towards a similar relationship across species despite differences in absolute rates.

To disentangle the effects of saccade rate and task condition, we fit a linear model predicting RCRI from average saccade rate and condition. In humans, saccade rate was a significant predictor of RCRI ($\beta = 0.0114$ per Hz, $P = 0.014$), whereas neither the IRREGULAR nor IMAGE condition differed from REGULAR once rate was accounted for. Thus, after controlling for saccade rate, task condition no longer explained additional variance in rhythmicity. Similar patterns were observed in macaques, where rate showed a strong positive effect on RCRI ($\beta = 0.146$ per Hz, $P = 0.026$), while condition effects were not significant. The marmoset data followed the same trend descriptively, although formal inference was not possible due to the limited sample size.

Together, these results demonstrate differences in RCRI across tasks and species. Intriguingly, while the RCRI metric corrects for slow rate fluctuations, the RCRI differences could be accounted for by differences in saccade rate. This suggests a genuine relation between saccade rate and saccade rhythmicity.

Saccade rhythmicity as function of saccade rate

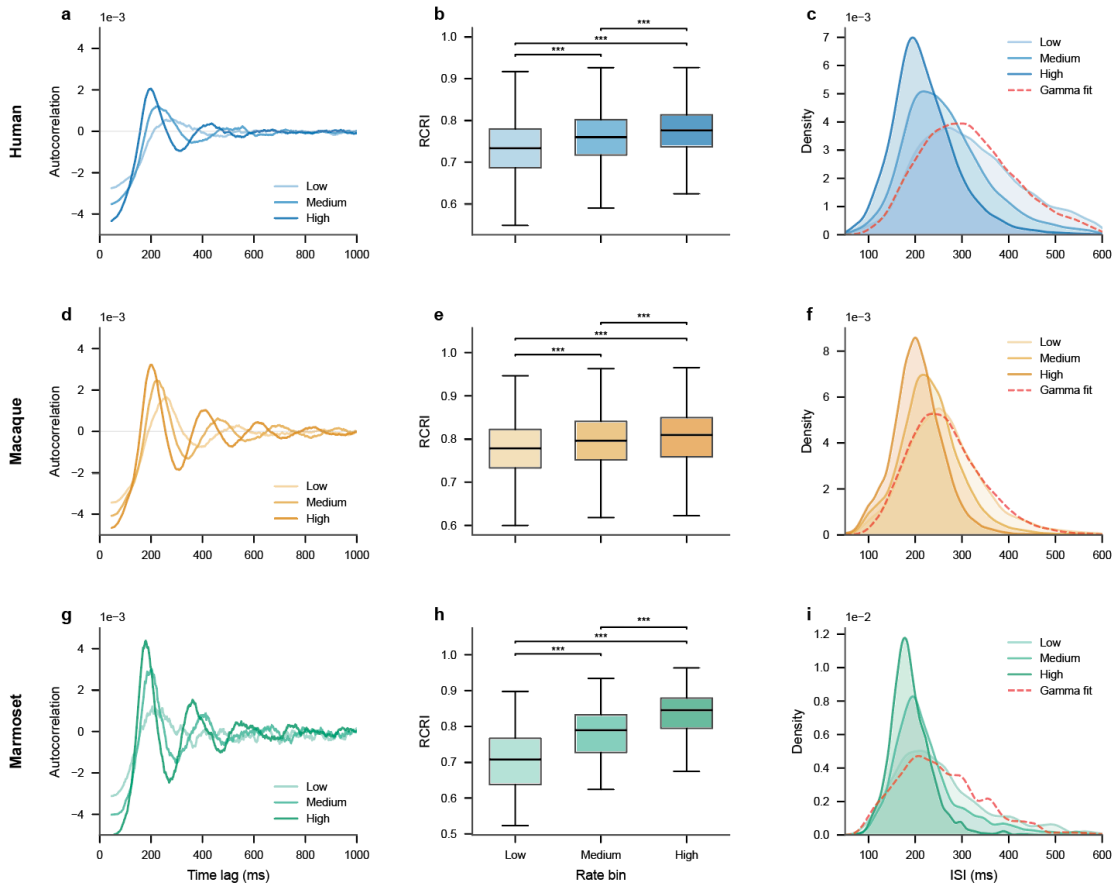

Figure 5. Rhythmic structure strengthens monotonically with saccade rate. (a, d, g) Autocorrelation functions of saccades for trials binned into low, medium, and high saccade-rate tertiles, shown separately for humans, macaques, and marmoset. Higher-rate trials exhibited more pronounced oscillatory side peaks. **(b, e, h)** RCRI across rate bins for each species. RCRI increases monotonically from low- to high-rate bins. **(c, f, i)** ISI distributions for the same rate bins. Increasing saccade rate is associated with shorter ISIs and narrower ISI distributions. We repeated the analysis of Figure 2 for the lowest saccade rate bin, and plotted the ISI distributions approximated via doubly stochastic gamma fit as red dashed lines. Even for the lowest rate bin, all gamma scale parameters are > 8, indicating substantial symmetry.

As an independent and nonparametric validation of the relationship between saccade rate and rhythmicity, we next binned trials by their mean saccade rate and assessed rhythmicity within these rate-defined trial subsets. For each species separately, trials were assigned to tertiles of saccade rate (low, medium, high) using quantile binning, ensuring equal numbers of trials per bin within species and controlling for baseline rate differences across species (see Figure. 1).

Across humans, macaques, and marmoset, higher-rate trials consistently exhibited stronger rhythmic structure in the autocorrelation function (Figure 5a,d,g). In all species, the high-rate bin showed the clearest side peaks at short lags, while rhythmic structure weakened progressively in the medium- and low-rate bins. Consistent with this pattern, RCRI showed robust, monotonic increases with saccade rate (Figure 5b,e,h). In humans, RCRI differed between all pairs of rate bins (high vs. medium: $t = 7.944$, $P = 2.55 \times 10^{-15}$; high vs. low:

$t = 18.082$, $P = 1.36 \times 10^{-68}$; medium vs. low: $t = 11.091$, $P = 5.86 \times 10^{-28}$). The same pattern was observed in macaques (high vs. medium: $W = 4.664$, $P = 3.10 \times 10^{-6}$; high vs. low: $W = 11.140$, $P = 8.01 \times 10^{-29}$; medium vs. low: $W = 6.980$, $P = 2.96 \times 10^{-12}$) and in the marmoset (high vs. medium: $W = 6.739$, $P = 1.59 \times 10^{-11}$; high vs. low: $W = 11.171$, $P = 5.67 \times 10^{-29}$; medium vs. low: $W = 6.793$, $P = 1.10 \times 10^{-11}$). Correspondingly, ISI distributions shifted systematically toward shorter ISIs and narrower distributions with increasing saccade rates (Figure 5c,f,i).

This rate-binned analysis provides converging evidence that saccade rhythmicity increases monotonically with saccade rate for each of the investigated primate species. Importantly, this conclusion is supported simultaneously by spectral analysis such as the structured side peaks in the autocorrelation function, by marginal measures such as systematic shifts in ISI distributions, and finally by the RCRI. Thus, the observed relationship between saccade rate and rhythmicity is not an artifact of a specific metric, modelling assumption, or analysis framework, but reflects a robust property of saccade timing across species.

Slow rate fluctuations induce higher-order temporal dependencies

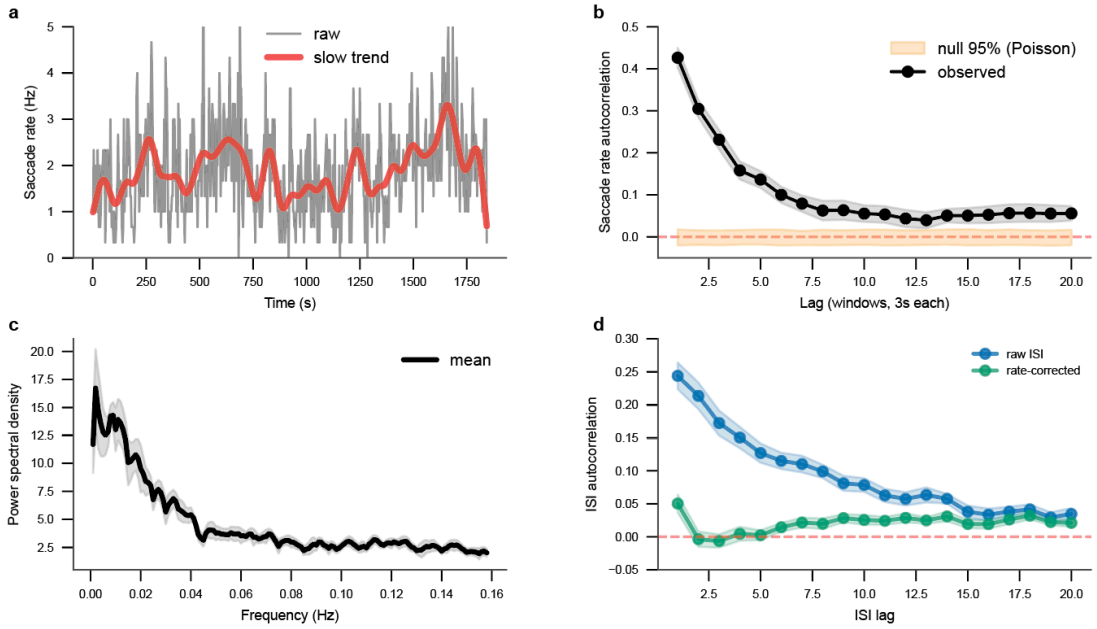

Figure 6. Slow rate fluctuations generate higher-order temporal dependencies. **(a)** Example saccade-rate time course from a single free-viewing MOVIE-condition trial, estimated in non-overlapping 3 s windows. Gray line shows raw windowed rates; red line shows a low-frequency trend illustrating slow rate drift over tens to hundreds of seconds. Note that the x-axis scale in panel a is in seconds. **(b)** Serial correlation of windowed saccade rate across trials (black, mean ± SEM across participants), compared to a Monte Carlo null envelope derived from stationary homogeneous Poisson processes (orange, 95% CI). Non-overlapping 3-second windows. **(c)** Power spectral density of windowed saccade rate (mean ± SEM across participants), showing concentration of power at very low frequencies, consistent with slow rate fluctuations. **(d)** Serial correlation of ISIs before (blue, mean ± SEM across participants) and after time-rescaling by the estimated time-varying rate (green, mean ± SEM across participants). Rate correction collapses ISI correlations toward zero across lags.

Having established that saccade rate varies substantially across trials (Figure 1), we next investigated saccade-rate dynamics during free viewing of the MOVIE condition in ≈30 min long uninterrupted trials. Figure 6a shows an example saccade-rate time course from a single free-viewing trial. Although instantaneous rate estimates were noisy, a pronounced component fluctuating on the timescale of tens to hundreds of seconds is evident. We quantified this temporal structure by computing the serial correlation of the windowed rate sequence (Figure 6b, see Methods for the relation between serial correlation and autocorrelation). This rate serial correlation was positive at short lags and decayed gradually with increasing lag, suggesting slow temporal structure. To verify that this effect did not arise trivially from estimating rate in finite windows, we calculated the serial correlation also for a Monte Carlo null model. Surrogate rate time series were generated from stationary homogeneous point processes with no rate drift, conditioned on the observed total number of saccades per trial and analyzed using the identical windowing and serial correlation procedure. Under this null model, expected rate serial correlation was close to zero at all lags, with a narrow 95% confidence envelope reflecting finite-sample variability (Figure 6b, orange). This null model did not show the empirical serial-correlation decay.

Spectral analysis of the rate time series further supported the presence of slow rate fluctuations. The power spectral density of the windowed rate estimates was dominated by very low frequencies and showed a ~1/f-like decay, with no distinct spectral peak (Figure 6c).

We investigated whether these slow rate fluctuations induced higher-order temporal dependencies in saccade timing. We computed the serial correlation of ISIs excluding intervals overlapping blinks. ISI serial correlation was positive across many lags (Figure 6d, blue), indicating that successive intervals are not independent. These higher-order dependencies extended well beyond adjacent intervals and decayed gradually with lag.

Critically, to test whether these ISI correlations reflect intrinsic structure of the saccade generator or are instead induced by the slow rate variability, we applied a time-rescaling transformation. Each ISI was converted from clock time to a rate-corrected measure by integrating the empirically estimated instantaneous rate over a 3 s analysis-window duration. This yielded the cumulative expected number of events during that interval, accounting for rate fluctuations. If dependencies arose solely from rate drift rather than intrinsic higher-order mechanisms, rescaled intervals should become approximately independent. After transformation, the serial correlation collapsed to values near zero across all lags (Figure 6d, green). This marked reduction demonstrates that the apparent higher-order dependencies in the ISI sequence are largely induced by slow fluctuations in saccade rate, rather than reflecting intrinsic temporal structure of the saccade generator itself. In other words, once rate fluctuations are accounted for, successive saccade intervals behave approximately as a renewal process: each interval depends only on the current rate, not on preceding intervals.

Together, these results show that saccade rates within long trials are non-stationary and exhibit slow, scale-free drifts that are not merely due to noisy ISI variation. This non-stationarity, specifically the slow rate drift, generates temporal structure in the ISI sequence.

Discussion

We explored the temporal dynamics of human, macaque, and marmoset saccades during a variety of different visual stimulation and task conditions. Across the three primate species performing matched free viewing visual foraging tasks, we find that saccade timings can be decomposed into regular rhythmic intervals and non-stationary rate modulation. First, saccade rates varied widely across trials and drifted slowly within long trials, implying that the empirical heavy-tailed ISI distributions are mixtures over many local regimes rather than signatures of unitary stationary processes. Consistent with this, a gamma-renewal model with a high shape parameter and time-varying rate reproduced the ISI heavy tail, and ISI distributions became more symmetric and narrower after normalizing for slow rate fluctuations. Second, we showed that slow rate fluctuations can strongly distort spectral indices of rhythmicity, attenuating peaks even when local regularity is unchanged and thereby confounding previously used peak-power based quantifications and interpretations of saccade rhythmicity. To address this, we introduced the RCRI that is largely invariant to slow rate drifts and then used it to compare saccade rhythmicity across tasks and species. With this metric, across-condition differences in rhythmicity were exclusively explained by differences in saccade rate. Non-parametric tests revealed a monotonic strengthening of rhythmicity with increasing rate for all three primate species. Finally, slow rate dynamics induced long-range serial correlations of ISIs, but these dependencies collapsed under time-rescaling, indicating that the dominant higher-order structure arises from smooth rate drift rather than intrinsic multi-interval dependence of the local generator. Together, these findings reconcile heavy-tailed ISIs and weak spectral peaks with a robust local rhythmic component whose expression is governed by how the oculomotor system modulates rate across time and context.

Several limitations to our findings should be noted. First, for the macaques and the marmoset, the sample sizes were two and one, respectively, such that the inference was limited to the sample rather than to the population[18]. Second, our conclusions are tied to the specific stimulus set and viewing regimes tested here (static arrays, natural images and relatively slow/smooth movie free viewing). Saccade statistics, including higher-order dependencies, may differ for stimuli and/or tasks with more pronounced temporal structure, or for other behavioral goals. Third, although the deep learning-based saccade detection is designed to be highly sensitive, rhythmicity and serial-correlation estimates can, in principle, be influenced by systematic detection biases, particularly for small-amplitude saccades and during free viewing where other eye-movement components such as smooth pursuits are present. Finally, our modelling framework is intentionally descriptive and based on behavioral data. It constrains the structure of the generative process but does not identify the underlying neuronal mechanism, motivating future work that links rate modulation and local rhythmicity to circuit-level dynamics.

The temporal structure of saccade sequences has a long history of empirical characterization and theoretical debate. Early work established that successive saccades cannot generally be initiated arbitrarily close in time. This post-saccadic refractory period imposes an apparent hard floor on the ISI, on the order of 100–200 ms [19,20] dictating the primary mode of the ISI distribution. Mechanistically, it was suggested by Carpenter and colleagues that this mode reflects the time for a threshold to be reached by a linearly accumulating decision signal with a stochastically varying rate, producing characteristically right-skewed reaction times (or ISI distributions) as a natural consequence of this variability[4,21]. Sumner and colleagues extended this view within neuronal field models to show that competitive fixation-saccade dynamics

further shape the tail[22]. Together, these frameworks converge on the view that the heavy-tailed ISI distribution is primarily a product of stochastic accumulation-to-threshold dynamics gated by a post-saccadic recovery period.

The most direct empirical evidence that saccade timing can nonetheless express a genuine local rhythmic component comes from the work of Otero-Millan and colleagues. Examining ISI distributions across saccade amplitude classes during both fixation and free exploration Otero-Millan et al. [23] showed that the statistics of successive events are consistent with a single common saccadic generator whose inter-event distributions share the same ex-Gaussian form regardless of saccade amplitude, with a mean of the Gaussian component near 150 ms and a heavy tail reflecting occasional prolonged intervals. The case for an intrinsically rhythmic generator becomes compelling in patients with square-wave jerks, spontaneous conjugate saccadic intrusions that interrupt fixation in paired saccades away from and back to a fixation location. Otero-Millan et al. [24,25] documented that the interval between these paired saccades converges tightly on approximately 200 ms, consistent with square waves observed in healthy individuals[26,27]. Rather than being merely an effect of pathology, these near-constant inter-saccadic periods could be understood as revealing, in unusually clean form, the local rhythmic kernel that the oculomotor system's intrinsic recovery dynamics impose. This kernel might normally be obscured in healthy free viewing by the superposition of rate variability, higher cognitive influences, or other sources of variability. This directly supports our finding that a robust rhythmic component is present in healthy primate saccade sequences once slow rate fluctuations are accounted for. Even when modelling how saccade generation is interrupted by sensory transients [16], successive saccade generation was an outcome of repetitive rise-to-threshold waves that could be reset by exogenous stimuli[28], again utilizing the concept of saccade-system rhythmicity.

Despite this rich tradition of characterizing saccade timing, none of these accounts set out to quantify saccade rhythmicity as such. To our knowledge, the only study that has considered this question directly is Amit et al., (2017), who explicitly asked whether free-viewing saccade sequences are better described by a self-paced generator or by a fixed-frequency oscillator, i.e., a central pattern generator. To answer this question, Amit et al. quantified spectral modulation strength, complemented by point-process analyses of autocorrelograms and hazard functions, and used ISI shuffling to test for dependencies beyond the immediately preceding saccade. In their data, hazard functions were dominated by post-saccadic inhibition without sustained periodic modulation, autocorrelograms showed at most short-lived damped structure, and shuffling left the oscillatory-modulation index largely unchanged. They concluded that a 3–6 Hz spectral peak is parsimoniously explained by first-order dynamics such as a post-saccadic refractory period, without invoking an autonomous pacemaker.

Our results extend this framework by showing that its core diagnostics can be confounded when saccade rate is non-stationary. Amit et al.'s generative models assume a constant base rate, and the ISI shuffle test is naturally interpreted in this stationary setting. In our data, saccade rate varies strongly across trials and drifts within them, so the empirical ISI distribution becomes a marginal distribution that pools intervals sampled at different prevailing rates. Rate modulation can therefore affect global timing statistics, masking spectral signatures typically attributed to rhythmicity. The same logic applies to the hazard function: locally present periodic modulation can be washed out by the mixture, yielding the flat or monotonically rising profiles that Amit et al. interpreted as evidence against an oscillatory process. Our simulations confirm that shuffling leaves peak power essentially unchanged not

only for stationary renewal data but also for non-stationary, rate-modulated data (Figure 3e), so a null shuffle effect does not uniquely support the inference that only first-order dependencies are present. By contrast, the RCRI is shuffle-invariant for stationary renewal data, but is disrupted by shuffling for non-stationary sequences (Figure 3f), because shuffling breaks the alignment between successive intervals and the slowly varying rate regime that generated them. These results do not contradict Amit et al.'s conclusion that saccade timing is poorly captured by a rigid, continuously phase-advancing oscillator, but extend their analysis to the regime that dominates natural viewing. When rate variability is accounted for, a local rhythmic component becomes evident, while much of the long-range ISI structure is explained by slow rate modulation.

Our descriptive model decomposes saccade timing into a local gamma-renewal generator and slow, empirically observed non-stationary rate modulation. Together, these two components account for the heavy-tailed marginal ISI distribution and for long-range serial dependencies that collapse under time-rescaling. The natural mechanistic question is which neuronal architecture could implement this decomposition. A parsimonious candidate is a drift-to-threshold mechanism. In this framework, after each post-saccadic reset, a decision variable accumulates toward a fixed threshold. At threshold crossing, a saccade is triggered, followed by a refractory period before the next build-up begins. Each cycle is analogous to one period of an oscillator, but the frequency is not fixed, it varies with the drift rate and the threshold level. This mechanism directly explains our central empirical finding that RCRI increases with mean saccade rate: If the noise of the accumulation process is approximately stable, increasing the mean drift compresses the time-to-threshold distribution and reduces relative dispersion, producing a more regular local sequence for shorter intervals (Figure 7).

This mechanistic explanation has strong neurophysiological grounding. In the frontal eye fields (FEF), movement-related neurons reach a relatively fixed discharge level at saccade onset, with latency variability explained by variability in the growth rate toward threshold[29]. Analogous threshold-crossing dynamics have been reported in the superior colliculus[30]. Downstream, the brainstem burst generator provides an explicit gating and refractory mechanism: omnipause neurons tonically inhibit premotor burst neurons during fixation and pause around saccades, naturally implementing a post-saccadic reset epoch and separating fast, local trigger timing from slower control signals that modulate readiness. Together, these circuits map onto our behavioral decomposition of a locally regular threshold-and-reset generator whose instantaneous rate is set by external drive.

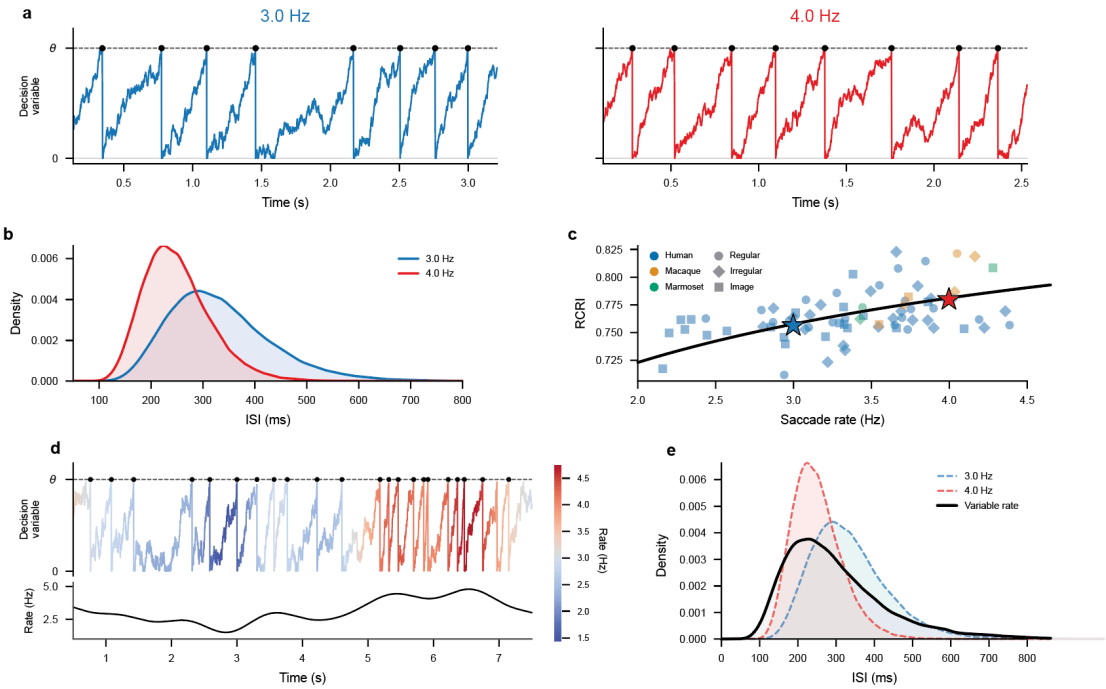

Figure 7. A drift-to-threshold model predicts the observed coupling between saccade rate and rhythmicity. (a) Example accumulator traces from a drift-to-threshold model at two drift rates (3.0 Hz, blue; 4.0 Hz, red). A decision variable accumulates with constant drift and Gaussian noise toward a fixed threshold (dashed line), triggering a saccade upon crossing. Higher drift produces faster saccade rates. **(b)** Inter-saccade interval (ISI) distributions for the two example rates. Higher drift yields a narrower, more regular ISI distribution, corresponding to higher rhythmicity. **(c)** Rate–RCRI relationship from Figure 4 predicted by the drift-to-threshold model (black line; single free parameter σ fitted to empirical data) overlaid on empirical data from humans (light blue), macaques (orange), and marmoset (green) across conditions. Stars indicate the two example rates from panels a and b. The model captures the monotonic increase of RCRI with saccade rate observed across species and conditions. **(d)** Accumulator trace driven by a slowly fluctuating rate signal, with color indicating instantaneous rate. The rate time course (bottom) varies smoothly between 2.0 and 4.5 Hz, producing epochs of faster and slower saccade generation. **(e)** ISI distribution from the variable-rate simulation (black) compared to the two constant-rate distributions from panel b (dashed). The variable-rate distribution emerges as a mixture of the underlying constant-rate distributions, demonstrating how slow rate fluctuations broaden the overall ISI distribution while preserving local rhythmicity.

The classic Linear Approach to Threshold with Ergodic Rate (LATER) framework assumes that the drift rate is drawn independently on each saccade cycle (or trial, in the classic LATER model), predicting no long-range serial structure in ISIs beyond the refractory period. The slow non-stationarity we observe violates this assumption: the rate does not reset independently after each saccade but instead shows serial correlation structure and therefore drifts continuously, such that successive cycles share a similar local rate context. This can be thought of as the signature of a system operating under slowly drifting control variables such as baseline excitability, urgency, exploration policy, tonic fixation drive, and neuromodulatory state, all of which change on timescales longer than a single ISI. Changes in these control variables might well correspond to different cognitive states, like levels of arousal, reward expectancy and resulting motivation[31–34].

Finally, this framework makes concrete predictions about how rate and local rhythmicity can dissociate. In drift-to-threshold terms, mean rate varies via the mean drift or the threshold level, whereas rhythmicity at matched rate is determined by the variability in drift, reset depth, or refractory gating. A central implication of this is that saccade timing during natural viewing can be viewed as the superposition of at least two timescales: a locally regular generator and slower, non-stationary rate modulation that reshapes global statistics. These timescales might in future studies be investigated during perturbation at various nodes of the saccade control and generation system, thereby identifying the neuronal bases behind the distinct behavioral components. At the neuronal level, saccade generation and attentional control are tightly intertwined. Thereby, a deeper understanding of the neuronal sources of saccade rhythmicity will also provide a link to the rich literature on rhythmicity in attentional and perceptual processes [7,35–37].

Acknowledgements

The authors would like to thank Ece Nur Uygur for help with the human data acquisition. This work was supported by DFG (FOR 1847 FR2557/2-1, FR2557/7-1, TH 425/17-1).

Author contributions:

T.N.: Conceptualization, Data curation, Formal analysis, Investigation, Methodology, Resources, Software, Visualization, Writing – original draft, Writing, review & editing. Y.Z.: Conceptualization, Formal analysis, Data curation, Investigation, Methodology, Resources, Software, Visualization, Writing – original draft, Writing, review & editing. S.P.: Investigation, Writing, review & editing. M.P.: Investigation, Writing, review & editing. L.B.: Conceptualization , Writing, review & editing. P.T.: Supervision, Funding acquisition, Writing, review & editing. Z.H.: Conceptualization, Methodology, Writing – original draft, Writing, review & editing. P.F.: Conceptualization, Supervision, Funding acquisition, Writing – original draft, Writing, review & editing.

Declaration of interests

P.F. has a patent on thin-film electrodes and is member of the Advisory Board of CorTec GmbH (Freiburg, Germany). T.N. was employed by Meta Platforms, Inc. during a portion of the preparation of this manuscript. The work reported here was conducted independently of Meta. T.N. is an inventor on a US Provisional Patent Application (Applicant: Meta Platforms, Inc.) related to human-computer interaction methods. The subject matter is unrelated to the work reported in this manuscript. The authors declare no further competing interests.

Declaration of generative AI and AI-assisted technologies in the manuscript preparation process

During the preparation of this work the authors used Claude Opus to aid with writing the manuscript. After using this tool, the authors reviewed and edited the content as needed and take full responsibility for the content of the published article.

References

1. Otero-Millan, J., Macknik, S.L., Langston, R.E., and Martinez-Conde, S. (2013). An oculomotor continuum from exploration to fixation. Proc. Natl. Acad. Sci. *110*, 6175–6180. https://doi.org/10.1073/pnas.1222715110.

2. Kleinfeld, D., Ahissar, E., and Diamond, M.E. (2006). Active sensation: insights from the rodent vibrissa sensorimotor system. Curr. Opin. Neurobiol. *16*, 435–444. https://doi.org/10.1016/j.conb.2006.06.009.

3. Takatoh, J., Prevosto, V., Thompson, P.M., Lu, J., Chung, L., Harrahill, A., Li, S., Zhao, S., He, Z., Golomb, D., et al. (2022). The whisking oscillator circuit. Nature *609*, 560–568. https://doi.org/10.1038/s41586-022-05144-8.

4. Noorani, I., and Carpenter, R.H.S. (2016). The LATER model of reaction time and decision. Neurosci. Biobehav. Rev. *64*, 229–251. https://doi.org/10.1016/j.neubiorev.2016.02.018.

5. Amit, R., Abeles, D., Bar-Gad, I., and Yuval-Greenberg, S. (2017). Temporal dynamics of saccades explained by a self-paced process. Sci. Rep. *7*, 886. https://doi.org/10.1038/s41598-017-00881-7.

6. Fiebelkorn, I.C., Saalmann, Y.B., and Kastner, S. (2013). Rhythmic Sampling within and between Objects despite Sustained Attention at a Cued Location. Curr. Biol. *23*, 2553–2558. https://doi.org/10.1016/j.cub.2013.10.063.

7. Fries, P. (2023). Rhythmic attentional scanning. Neuron *111*, 954–970. https://doi.org/10.1016/j.neuron.2023.02.015.

8. Landau, A.N., and Fries, P. (2012). Attention samples stimuli rhythmically. Curr. Biol. CB *22*, 1000–1004. https://doi.org/10.1016/j.cub.2012.03.054.

9. Tian, X., Yoshida, M., and Hafed, Z.M. (2016). A Microsaccadic Account of Attentional Capture and Inhibition of Return in Posner Cueing. Front. Syst. Neurosci. *10*. https://doi.org/10.3389/fnsys.2016.00023.

10. Bellet, J., Chen, C.-Y., and Hafed, Z.M. (2017). Sequential hemifield gating of α- and β-behavioral performance oscillations after microsaccades. J. Neurophysiol. *118*, 2789–2805. https://doi.org/10.1152/jn.00253.2017.

11. Benedetto, A., and Morrone, M.C. (2017). Saccadic Suppression Is Embedded Within Extended Oscillatory Modulation of Sensitivity. J. Neurosci. Off. J. Soc. Neurosci. *37*, 3661–3670. https://doi.org/10.1523/JNEUROSCI.2390-16.2016.

12. Bellet, M.E., Bellet, J., Nienborg, H., Hafed, Z.M., and Berens, P. (2019). Human-level saccade detection performance using deep neural networks. J. Neurophysiol. *121*, 646–661. https://doi.org/10.1152/jn.00601.2018.

13. Reingold, E.M., and Stampe, D.M. (2000). Saccadic inhibition and gaze contingent research paradigms. In Reading as a perceptual process (North-Holland/Elsevier Science Publishers), pp. 119–145. https://doi.org/10.1016/B978-008043642-5/50008-5.

14. Engbert, R., and Kliegl, R. (2003). Microsaccades uncover the orientation of covert attention. Vision Res. *43*, 1035–1045. https://doi.org/10.1016/s0042-6989(03)00084-1.

15. Fries, P., Womelsdorf, T., Oostenveld, R., and Desimone, R. (2008). The effects of visual stimulation and selective visual attention on rhythmic neuronal synchronization in macaque area V4. J. Neurosci. Off. J. Soc. Neurosci. *28*, 4823–4835. https://doi.org/10.1523/JNEUROSCI.4499-07.2008.

16. Buonocore, A., and Hafed, Z.M. (2023). The inevitability of visual interruption. J. Neurophysiol. *130*, 225–237. https://doi.org/10.1152/jn.00441.2022.

17. Holt, G.R., Softky, W.R., Koch, C., and Douglas, R.J. (1996). Comparison of discharge variability in vitro and in vivo in cat visual cortex neurons. J. Neurophysiol. *75*, 1806–1814. https://doi.org/10.1152/jn.1996.75.5.1806.

18. Fries, P., and Maris, E. (2022). What to Do If N Is Two? J. Cogn. Neurosci. *34*, 1114–1118. https://doi.org/10.1162/jocn_a_01857.

19. Hallett, P.E., and Lightstone, A.D. (1976). Saccadic eye movements towards stimuli triggered by prior saccades. Vision Res. *16*, 99–106. https://doi.org/10.1016/0042-6989(76)90083-3.

20. Hallett, P.E., and Adams, B.D. (1980). The predictability of saccadic latency in a novel voluntary oculomotor task. Vision Res. *20*, 329–339. https://doi.org/10.1016/0042-6989(80)90019-X.

21. Carpenter, R.H.S., and Williams, M.L.L. (1995). Neural computation of log likelihood in control of saccadic eye movements. Nature *377*, 59–62. https://doi.org/10.1038/377059a0.

22. Bompas, A., and Sumner, P. (2011). Saccadic Inhibition Reveals the Timing of Automatic and Voluntary Signals in the Human Brain. J. Neurosci. *31*, 12501–12512. https://doi.org/10.1523/JNEUROSCI.2234-11.2011.

23. Otero-Millan, J., Troncoso, X.G., Macknik, S.L., Serrano-Pedraza, I., and Martinez-Conde, S. (2008). Saccades and microsaccades during visual fixation, exploration, and search: Foundations for a common saccadic generator. J. Vis. *8*, 21–21. https://doi.org/10.1167/8.14.21.

24. Otero-Millan, J., Schneider, R., Leigh, R.J., Macknik, S.L., and Martinez-Conde, S. (2013). Saccades during Attempted Fixation in Parkinsonian Disorders and Recessive Ataxia: From Microsaccades to Square-Wave Jerks. PLOS ONE *8*, e58535. https://doi.org/10.1371/journal.pone.0058535.

25. Otero-Millan, J., Serra, A., Leigh, R.J., Troncoso, X.G., Macknik, S.L., and Martinez-Conde, S. (2011). Distinctive features of saccadic intrusions and microsaccades in progressive supranuclear palsy. J. Neurosci. Off. J. Soc. Neurosci. *31*, 4379–4387. https://doi.org/10.1523/JNEUROSCI.2600-10.2011.

26. Hafed, Z.M., and Clark, J.J. (2002). Microsaccades as an overt measure of covert attention shifts. Vision Res. *42*, 2533–2545. https://doi.org/10.1016/S0042-6989(02)00263-8.

27. Hafed, Z.M., and Ignashchenkova, A. (2013). On the Dissociation between Microsaccade Rate and Direction after Peripheral Cues: Microsaccadic Inhibition Revisited. J. Neurosci. *33*, 16220–16235. https://doi.org/10.1523/JNEUROSCI.2240-13.2013.

28. Hafed, Z.M., and Ignashchenkova, A. (2013). On the dissociation between microsaccade rate and direction after peripheral cues: microsaccadic inhibition revisited. J. Neurosci. Off. J. Soc. Neurosci. *33*, 16220–16235. https://doi.org/10.1523/JNEUROSCI.2240-13.2013.

29. Hanes, D.P., and Schall, J.D. (1996). Neural control of voluntary movement initiation. Science *274*, 427–430. https://doi.org/10.1126/science.274.5286.427.

30. Dorris, M.C., Paré, M., and Munoz, D.P. (1997). Neuronal Activity in Monkey Superior Colliculus Related to the Initiation of Saccadic Eye Movements. J. Neurosci. *17*, 8566–8579. https://doi.org/10.1523/JNEUROSCI.17-21-08566.1997.

31. Bray, T.J.P., and Carpenter, R.H.S. (2015). Saccadic foraging: reduced reaction time to informative targets. Eur. J. Neurosci. *41*, 908–913. https://doi.org/10.1111/ejn.12845.

32. Milstein, D.M., and Dorris, M.C. (2007). The Influence of Expected Value on Saccadic Preparation. J. Neurosci. *27*, 4810–4818. https://doi.org/10.1523/JNEUROSCI.0577-07.2007.

33. Milstein, D.M., and Dorris, M.C. (2011). The Relationship between Saccadic Choice and Reaction Times with Manipulations of Target Value. Front. Neurosci. *5*. https://doi.org/10.3389/fnins.2011.00122.

34. Prsa, M., Dicke, P.W., and Thier, P. (2010). The absence of eye muscle fatigue indicates that the nervous system compensates for non-motor disturbances of oculomotor function. J. Neurosci. Off. J. Soc. Neurosci. *30*, 15834–15842. https://doi.org/10.1523/JNEUROSCI.3901-10.2010.

35. Bosman, C.A., Schoffelen, J.-M., Brunet, N., Oostenveld, R., Bastos, A.M., Womelsdorf, T., Rubehn, B., Stieglitz, T., De Weerd, P., and Fries, P. (2012). Attentional Stimulus Selection through Selective Synchronization between Monkey Visual Areas. Neuron *75*, 875–888. https://doi.org/10.1016/j.neuron.2012.06.037.

36. Hafed, Z.M. (2013). Alteration of Visual Perception prior to Microsaccades. Neuron *77*, 775–786. https://doi.org/10.1016/j.neuron.2012.12.014.

37. Landau, A.N., Schreyer, H.M., van Pelt, S., and Fries, P. (2015). Distributed Attention Is Implemented through Theta-Rhythmic Gamma Modulation. Curr. Biol. *25*, 2332–2337. https://doi.org/10.1016/j.cub.2015.07.048.